ЭACEE

JACEE EMULSION CHAMBERS FOR STUDYING THE ENERGY SPECTRA OF HIGH ENERGY COSMIC RAY PROTONS AND HELIUM *

The JACEE Collaboration **

T.H. BURNETT [j], S. DAKE [b], M. FUKI [c], J.C. GREGORY [h], T. HAYASHI [d,h], R. HOLYNSKI [k], J. IWAI [j], W.V. JONES [f], A. JURAK [k], J.J. LORD [j], O. MIYAMURA [c], H. ODA [b], T. OGATA [a], T.A. PARNELL [g], T. SAITO [a], T. TABUKI [a], Y. TAKAHASHI [g,i], T. TOMINAGA [c], J.W. WATTS [g], B. WILCZYNSKA [k], R.J. WILKES [j], W. WOLTER [k] and B. WOSIEK [i,k]

[a] Institute for Cosmic Ray Research, University of Tokyo, Tokyo 188, Japan
[b] Department of Physics, Kobe University, Kobe 657, Japan
[c] Department of Applied Mathematics, Osaka University, Osaka 560, Japan
[d] Science and Engineering Research Laboratory, Waseda University, Tokyo 162, Japan.
[e] Department of Physics, Okayama University of Science, Okayama 700, Japan.
[f] Department of Physics and Astronomy, Louisiana State University, Baton Rouge, LA 70803-4001, USA.
[g] Space Science Laboratory, NASA Marshall Space Flight Center, ES-62, Huntsville, AL 35812, USA.
[h] Department of Chemistry, University of Alabama, Huntsville, AL 35899, USA.
[i] Department of Physics, University of Alabama, Huntsville, AL 35899, USA.
[j] Visual Techniques Laboratory, University of Washington, Seattle, WA 98105, USA.
[k] Institute for Nuclear Physics, 30-055 Krakow, Poland.

Emulsion chambers are being used in a series of stratospheric balloon flights to study nuclear interactions, charge composition, and energy spectra of cosmic ray nuclei over the energy range $10^{12}-10^{15}$ eV. Charge identification involves grain, gap, and/or delta-ray counting in emulsion plates having different sensitivities on two sides of an acrylic base. Electromagnetic cascade energies are measured with resolutions of about 25% by the three-dimensional track counting method. This report describes the apparatus, the measurement techniques, and the analysis methods used to determine the primary proton and helium spectra.

1. Introduction

The Japanese–American Cooperative Emulsion Experiment (JACEE) is studying the interactions [1] and energy spectra [2] of cosmic ray nuclei at energies above ~ 1 TeV/nucleon. The data are recorded with balloon-borne emulsion chambers, which in one flight were combined with multiple counter systems. Emulsion chambers offer large effective geometrical aperature per unit weight, easy detection of high energy events, and high spatial resolution of the recorded data [3]. Their utility is illustrated by the JACEE exposures, in which data collected in only two balloon flights have been sufficient to extend the proton spectrum from a few TeV to several hundred TeV [2].

The only direct measurements previously reported on cosmic ray spectra above a few TeV were those carried out more than a decade ago by the PROTON satellites [4], in which an ionization calorimeter employing scintillators was used to make observations above 40 GeV. Those measurements extended up to about 2 TeV for helium, 20 TeV for protons, and 10^{16} eV for "all particles". (Individual charges heavier than helium were not resolved.) It was reported that the helium and all-particle spectra obeyed a simple power law over the energy range covered, but that the proton integral spectral index changed abruptly from −1.7 to −2.3 around 2 TeV. At the lower energies, balloon observations [5,6] were in agreement with the PROTON satellite results, but JACEE is the first balloon experiment to have sufficient exposure to make spectral measurements beyond the region of the reported index change for protons.

The emulsion chamber method is especially useful for ultrahigh energy cosmic ray observations, because (1) the efficiency for detecting interactions approaches 100% above about 10 TeV and (2) the energy resolution

is approximately constant with energy for a given inci-
dent particle species. Most other energy measuring tech-
niques are impractical for balloon observations of
primary cosmic rays at such high energies. For example,
the signals from low pressure gas Cherenkov counters
and transition radiation detectors become saturated,
and ionization calorimeters employing scintillators have
a much smaller geometrical factor than an emulsion
chamber of the same weight. In addition to the practical
limitations of the energy measuring technique, the en-
ergy range of all cosmic ray experiments is limited by
the collecting power (product of the geometrical factor
of the apparatus and the time of exposure to the cosmic
ray flux) and the steep energy spectra of primary cosmic
rays [5-7].

2. Apparatus

The basic, vertical configuration of the emulsion
chambers used in JACEE is illustrated schematically in
fig. 1. Each chamber is composed of four sections: the
primary charge detector, the target, the spacer, and the
calorimeter.

The primary charge detector contains both thick
(200-400 μm) and thin (50-100 μm) nuclear emulsions,
as well as CR-39 and Lexan solid state track detectors
[8]. The thick emulsions permit accurate determination
of the charge ($\Delta Z \approx (0.1-2)e$ for $Z = 1-26$) of each
primary particle via track grain density, gap length
distribution, and delta ray counts in emulsion layers of
different sensitivies. For heavy nuclei, the emulsion
charge measurements can be augmented by data from
the Lexan and CR-39 sheets.

The target section employs about fifty thin emulsion
plates interleaved with low-Z material (acrylic) to maxi-
mize the nuclear interaction probability, while minimiz-
ing the probability for pair production by high energy
photons. Charged tracks produced at an interaction
vertex in the ~1 mm thick acrylic plates can be ob-
served in the nearby emulsions. In order to identify
nuclear fragments, some charge identification layers
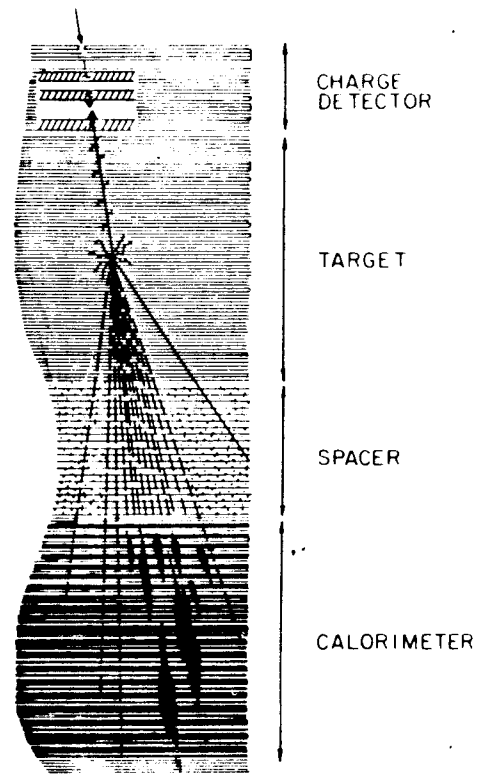(similar to those in the primary section) are inserted at

Fig. 1. Schematic diagram of the JACEE emulsion chambers.
The JACEE-0 and JACEE-2 chambers did not have the spacer
section.

regular intervals of about 3 cm throughout the target.
Table 1 shows the number of track-sensitive layers in
each section and specifies the typical section thicknesses
in centimeters, radiation lengths (r.l.), and proton inter-
action mean free paths. The target section has a vertical
thickness of approximately 0.25 proton interaction
lengths, which corresponds to about 1.0 interaction
length for iron nuclei.

The spacer section is a drift space comprised of
paper honeycomb that permits closely collimated gamma
rays from an upstream vertex to diverge from each

Table 1
Component thicknesses of the JACEE-1 chamber

Section	Plates	cm	g/cm^2	r.l.	Proton interaction lengths
Primary	10 Emul, 4 CR-39	1.78	3.38	0.17	0.035
Target	57 Emul, 8 CR-39, 46 plastic	15.92	22.00	0.77	0.263
Spacer	20 Emul	12.08	4.85	0.24	0.052
Calorimeter	22 Emul, 26 X-ray, 1 CR-39 [a]	6.30	43.38	6.12	0.244
Total		36.08	73.61	7.30	0.594

[a] Includes test processing materials exposed at the bottom of the chamber.

other before cascade development in the downstream calorimeter. A 10 cm drift space is adequate for separating 1 TeV gamma rays from neutral pion decay. Thin emulsion plates are inserted at intervals of about 5 mm throughout the spacer section, in order to facilitate the tracing process and to allow measurement of charged particle emission angles as small as 10^{-5} rad.

The calorimeter section has about 7 r.l. vertical thickness of lead absorber. The lead sheets, 1 mm and 2.5 mm thick, are interleaved with X-ray films and thin emulsion plates. High energy nuclear-electromagnetic cascades produce easily visible dark spots in the X-ray films. The X-ray film images are used both for naked-eye scanning to detect the events and for initial energy estimation by optical photometry. Each Sakura-type N X-ray film consists of 25 μm thick emulsion layers on both sides of a 175 μm polyester base.

Surviving heavy fragments, charged hadrons, and cascade electrons are observed individually in the emulsions, which are also used to determine the energies of electromagnetic cascades by the method of track counting. The emulsion plates consist of 50–400 μm thick layers of Fuji nuclear emulsion coated on both sides of either 500 or 800 μm thick acrylic base plates. The optical transparency of the acrylic base allows observations on both emulsion layers with the same microscope stage setting.

The double-coating technique, because of the dimensional stability of the base material and the capability of viewing both surfaces with a microscope, permits accurate measurements of track coordinates even though the emulsion may suffer shrinkage and distortion during processing. As discussed below (sect. 4), the use of different sensitivity emulsions on opposite sides of a base plate facilitates identification of vertically incident protons, helium, and lithium nuclei, which has been difficult in previous emulsion chamber applications.

All components of the chamber are assembled in 40 × 50 cm^2 precision-machined, light-tight, plastic boxes, which ensure that adjacent plates are aligned with an accuracy better than 150 μm. In one case (JACEE-2) a single 80 × 100 cm^2 box was used to hold four 40 cm × 50 cm^2 units, but this resulted in poorer (~ 1 mm) alignment.

The chambers are typically mounted in a "flipper" mechanism that keeps them inverted except while at float altitude, but in two flights a "plate shifter" was used. Either technique permits discrimination of interactions registered at the top of the atmosphere from those recorded at sea level or during balloon ascent and descent. The ability to reject low altitude background from the high altitude "live time" exposure is vital in measurements of the rare primary Li, Be, and B nuclei, and it would also be important for measurements of galactic electrons and gamma rays.

Table 2 lists some relevant parameters of the emulsion chambers for the six JACEE flights to date: JACEE-0, JACEE-1, JACEE-2, JACEE-3, JACEE-4 and JACEE-5. The first flight, JACEE-0, was a small-scale engineering flight carried out in Japan. Electronic counters were combined with the emulsion chamber in JACEE-3.

3. Event detection, selection, and tracing

The events are detected by observation of dark spots produced by cascades in the X-ray films of the calorimeter. Individual electromagnetic cascades of energy E_γ greater than about 300 GeV can produce spots visible to the naked eye. After an event has been found in the X-ray films, associated cascades with energies above about 50 GeV can be found by microscope scanning in the emulsions. The detection threshold for total gamma ray energy, ΣE_γ, can be as high as 1 TeV, because the cascade family associated with the event has several

Table 2
Balloon flights

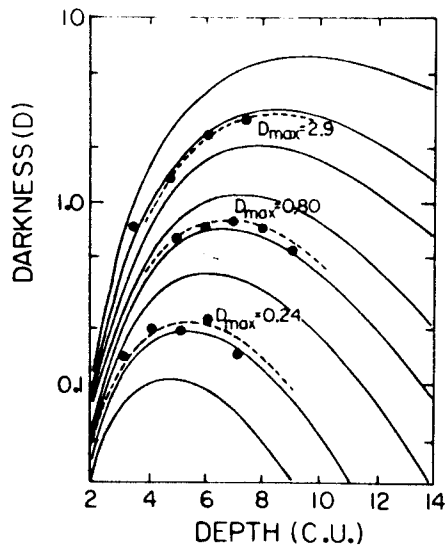| Flight	Launch date	Launch site	Altitude [g/cm^2]	Duration [h]	Area [cm^2]
JACEE-0	5/79	Sanriku, Japan	8.0	29.0	1(40 × 50)
JACEE-1	9/79	Palestine, Texas	3.7	25.2	4(40 × 50)
JACEE-2	9/80	Palestine, Texas	4.0	29.6	4(40 × 50)
JACEE-3	6/82	Greenville, S. Carolina	5.0	39.0	1(50 × 50)
JACEE-4	9/83	Palestine, Texas	5.0	59.5	4(40 × 50)
JACEE-5	10/84	Palestine, Texas	5.0	15.0	4(40 × 50)

Fig. 2. Longitudinal development of the optical density (D) in X-ray films for cascades initiated by protons. The maximum value (D_{max}) is used for the selection of events for analysis.

members each with $E_\gamma < 300$ GeV. The actual detection threshold (E_{th}) is a function of the incident angle of the event and the background level, which depends on both the freshness of the X-ray films and the processing variables.

Either optical densitometry in the X-ray films or track counting in emulsions around the cascade maximum provides an initial estimate of ΣE_γ, which serves as the preliminary parameter for selecting events for analysis. The D_{max} of individual events is defined by the optical density at the cascade maximum which is obtained by fitting optical densities measured at several layers to the shower curves (fig. 2). In practice, an optical density threshold of $D_{max} = \log_{10} I_0/I \geq 0.2$ is used, where I_0 and I respectively denote the source and the transmitted light intensities in the optical photometer. Scatter plots of photometric density of X-ray film spots (a measure of the total "pulse height") versus ΣE_γ from track counts in emulsion indicate a spread of about 40% for 2 TeV $< \Sigma E_\gamma < 20$ TeV (figs. 3a and b). This value includes the contributions from successive interactions in the calorimeter. Typically, the highest energy events are selected for earliest analysis, and the lower energy events are analyzed as time and manpower permit.

Following selection, the coordinates of dark spots in the X-ray films are mapped directly onto the adjacent emulsion plates, and the cascades are located using a microscope. Zenith (θ) and azimuth (ϕ) angles for the event are then determined from the entrance and exit points of individual particles (high energy photons and/or heavy nuclear fragments) in the acrylic base of
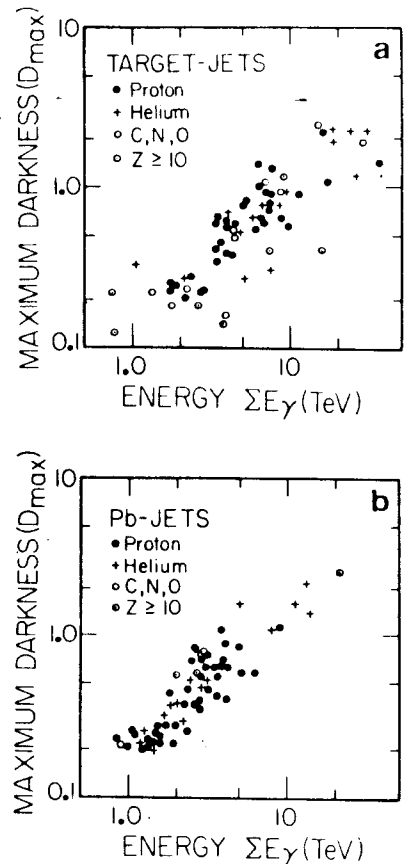

Fig. 3. Correlations of the maximum optical density (D_{max}) of X-ray films with measured cascade energy (ΣF_γ) for interaction events in the target section (target jets) (a) and in the calorimeter section (Pb jets) (b).

the emulsion plate. The angular accuracy ($\Delta\tan \theta < 0.01$ and $\Delta\phi < 0.2°$) facilitates tracing the cascade (and its accompanying charged hadrons and nuclear fragments) back to the interaction vertex. If a large number of particles are present, the traceback can be accomplished by making observations in only every fifth to tenth plates.

The traceback procedure is continued until the primary vertex is located, either by direct observation in an emulsion or (more frequently) by triangulated convergence of tracks to a point in a non-emulsion target plate or other nonsensitive layer. The convergence of the obvious cone of charged secondary particles in the emulsion plates immediately below the interaction usually fixes the vertex to within 100 μm. If wide-angled ($\theta \approx 1°-10°$) tracks are present in the nearest emulsion layer, the vertex can be located even more accurately, generally to within 50 μm.

A vertex is presumed to be a primary interaction if no accompanying parallel tracks are found within a radius of about 125 μm of the primary track in the

upstream emulsion plates. Background heavy nucleus tracks are often used as temporary fiducials for plate-to-plate scanning, particularly for proton and helium primaries, in order to ensure correct association of the primary particle with the vertex.

Although the overall tracing efficiency is estimated to be about 98%, a vertex is not found for every event during the tracebacks. In some cases the cascade begins as a narrow, low multiplicity jet where central tracks exhibit the multiple scattering characteristics of electrons rather than the more persistent trajectories associated with charged hadrons. Such events are classified as electromagnetic in origin. Fewer than 2% of the events are lost during tracing.

4. Charge measurements

Several methods are used, either individually or in combination, for determining the charge Z of each primary nucleus. Different methods are required for different charge groups, and the specific procedure depends on the angle of incidence. The approximate Z value is easily assigned at first glance under a microscope as being either a proton, a He nucleus, a light medium nucleus ($Z = 6-8$), or a heavy nucleus ($Z \geq 9$).

The use of low sensitivity emulsion permits grain counting even for nearly vertically incident tracks [9]. The track registration properties of the three different sensitivity emulsions employed (Fuji 7B, Fuji 6B, and Fuji 2F) are given in table 3, while table 4 shows the pairings of the different emulsion types used to make plates for specific experimental objectives, e.g., identification of the primary particle species.

Protons and helium are clearly separated, even for nearly vertical incidence, by the method of grain counting in emulsion plates having different sensitivities on the two sides of the acrylic base. For light nuclei, gap measurements in electron sensitive emulsions (Fuji 7B) and grain counting in reduced-sensitivity emulsions (Fuji 6B and Fuji 2F) are used. For medium and heavy nuclei, delta ray counts are combined with CR-39 etch-pit measurements.

The use of low sensitive emulsion makes grain counting possible for nearly vertical incident tracks. The

Table 3
Track registration properties of Fuji emulsion

Emulsion type	Particle track sensitivity		
	Electrons	Protons	Alpha particles
Fuji 7B	all	all	all
Fuji 6B	< 0.1 MeV	< 200 MeV	all
Fuji 2F	none	< 20 MeV	< 500 MeV

Table 4
JACEE emulsion plates. All plates are coated on both sides of either 500 or 800 μm methacrylate base with Fuji emulsion as specified

Plate type	Emulsion coating upper/lower	Layer thickness [μm]	Particle identification/purpose
A	7B/7B	200	p, alpha
B	7B/6B	200	alpha, light nucleus
C	7B/7B	50-75	track coordinates and angle
D	7B/2F	200	medium, heavy nucleus
E	7B/6B	400	medium, heavy nucleus

grain density (ρ_g), or more exactly, the blob density (which is the number of separated grains, or unresolved clumps of grains, per unit track length) is used to measure the ionization rate. Tracks are viewed in a vertical projection, and the vertical microscope resolution ($\epsilon_v = 1$ μm) is poorer than the horizontal resolution ($\epsilon_h = 0.12$ μm). The grain size (0.27 μm for Fuji 7B and 6B emulsions, and 0.17 μm for Fuji 2F emulsion) is comparable to the microscope resolution of gaps between grains, so more grains are unresolvable for steeper tracks.

The distribution of gap length between grains for a unit length is given by [10]

$$H(\Gamma) \, d\Gamma = \Gamma_0^{-2} \exp(-\Gamma/\Gamma_0) \, d\Gamma, \tag{1}$$

where Γ_0 denotes the average gap length, which is equivalent to the inverse of the grain density ρ. Their charge dependences can be reasonably assumed as $\Gamma_0(Z) = Z_{ef}^{-2}\Gamma_0(Z = 1)$, or $\rho(Z) = \rho_0 Z^2$. The measured number of separable grains or blobs N_b for a track length L therefore defines the blob density ρ_{blob}, and is related to the minimum grain density ρ_0 by

$$\rho_{blob} \equiv (N_b - 1)/L = \int_{\Gamma'}^{\infty} \rho^2 \exp(-\rho\Gamma) \, d\Gamma$$

$$= \rho_0 Z^2 \exp(-\rho_0 Z^2 \Gamma'), \tag{2}$$

where Γ' denotes the minimum resolvable gap length, and depends on the microscope resolution, $\Gamma' = \min\{\epsilon_v/\cos\theta, \epsilon_h/\sin\theta\}$.

Fig. 4 shows the observed distribution of blob density for 333 relativistic singly charged tracks having $\tan\theta = 0.5$ in one layer of 50 μm thick type 7B emulsion. The blob density and its dispersion are 31.9 ± 5.7 blobs/100 μm. From eq. (2) with $\epsilon_h = 0.12$ and $\sin\theta = 0.45$, the median and its statistical error of the grain density for a singly charged particle (ρ_0) in 7B emulsion is estimated to be 35.0 ± 0.4 grains per 100 μm. The corresponding median values of grain densities of proton tracks in 6B and 2F emulsions are also estimated by the same method as 13.1 ± 1 and 9.6 ± 1 per 100 μm, respectively.
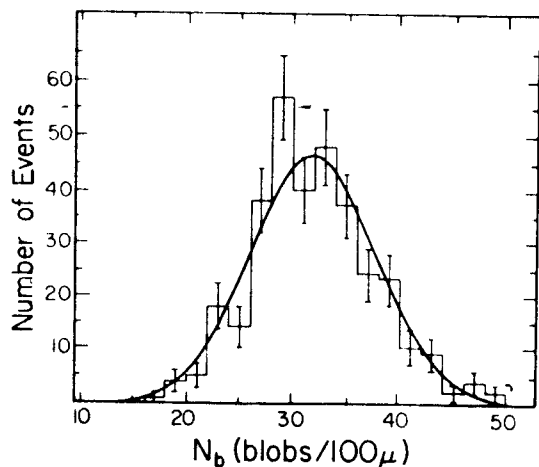
Fig. 4. Observed distribution of blob density for 333 singly charged relativistic tracks in Fuji 7B emulsion. The solid curve represents a Gaussian distribution with mean 31.9 and standard deviation 5.7 blobs/100 μm.
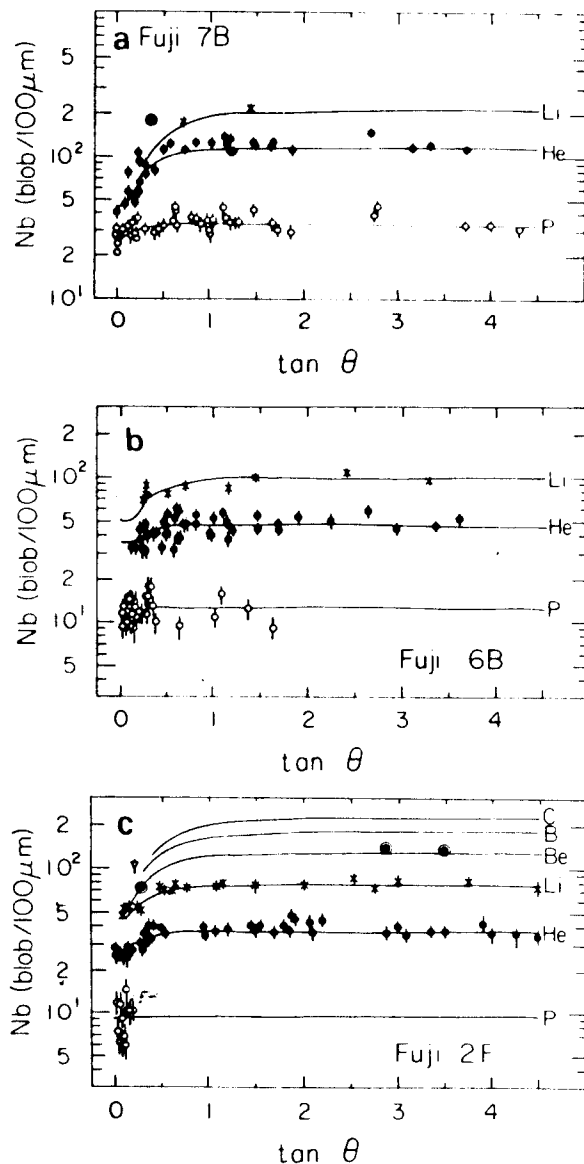

Fig. 5. Comparison of measured and calculated blob densities for proton, helium, and lithium tracks as a function of zenith angle for Fuji 7B (a), 6B (b) and 2F (c) emulsions.

Figs. 5a–c compare some JACEE data with expected blob densities from eq. (2) for p, He, and Li tracks in Fuji 7B, 6B, and 2F emulsions as a function of zenith angle. The data points are consistent with calculations using $\epsilon_v = 0.8$ μm and $\epsilon_h = 0.12$ μm.

Due to the reduction in the number of resolvable grains, identification of p and He for tan $\theta < 0.25$ and separation of He and Li nuclei for tan $\theta < 0.5$ are ambiguous in electron-sensitive 7B emulsion. However, by using reduced sensitivity 6B and 2F emulsions, unique separations of these light nuclei are made possible for almost all zenith angles. Nearly 100% discrimination of p and He is possible in a 7B/6B or 7B/2F combination emulsion plate, because a steep He in 6B or 2F emulsion leaves a track similar to that of a proton in 7B emulsion, while a proton does not produce an obvious track in the low sensitivity 6B and 2F emulsions.

Separation of He and Li for tan $\theta < 0.1$ is verified by the gap counting method. Provided the minimum (projected) gap length considered is much greater than the grain size, the grain density, $\rho_0 Z^2$, can be determined by measuring the gap length distribution for two or more different values of Γ'. This method is useful up to $Z = 6$ in 7B emulsion and up to $Z = 10$ in 6B emulsion, although longer track lengths are needed to get sufficient statistics for larger gap lengths.

The charge resolution (σ) of p and He by these methods is better than $\Delta Z = 0.1$ for $\theta > 30°$ and better than $\Delta Z = 0.2$ for all angles. Greater accuracy can be achieved by continuing the measurements in several consecutive plates.

Delta ray density measurements are used if only a few or no gaps are visible, i.e., for medium and heavy nuclei tracks. A delta ray is operationally defined as a

"whisker" of four or more grains attached to a heavy track. This widely used convention [9] corresponds to mean delta ray energies greater than about 15 keV. The number of delta rays is approximately proportional to Z^2 for relativistic nuclei, and for this convention there are approximately 3.8 delta rays per 100 μm for a $Z = 6$ track in Fuji 7B emulsion.

For nearly vertical tracks of heavy nuclei, accurate delta ray counts are difficult, because of the overlapping views of delta rays. In such cases, the etch-pit measurement in CR-39 provides easy and accurate charge determinations for vertical tracks of heavy ($Z > 6$) nuclei

[11]. For the latter method, the Z threshold increases and the resolution becomes poorer at larger zenith angles, because of the competition between the bulk etch rate and the track etch rate. The combination of emulsion and CR-39 charge measurement techniques augment each other to cover the full charge range ($Z = 1$–26) for all angles from $0°$ to $90°$. The charge resolutions for an iron nucleus using the delta ray and etch-pit methods in this experiment are. respectively, $\Delta Z = 2$ and $\Delta Z = 0.5$.

5. Energy measurements

In emulsion chamber experiments the part of the primary energy going into gamma-rays, ΣE_γ, is the parameter most easily related to the primary cosmic ray energy spectrum. Measurements that rely on the distributions of emission angles (θ'_{ch}) of secondary charged particles through the conventional energy estimation formula $\Sigma E_{ch} = \Sigma_i \langle P_T \rangle / \theta'_{ch}$, where $\langle P_T \rangle$ denotes the average transverse momentum (approximately 400 MeV/c), or the total estimated energy $E_0 = \Sigma E_\gamma + k \Sigma E_{ch}$ are less practical for primary energy spectrum studies.

Measurements of ΣE_γ in an emulsion calorimeter are made by two separate methods, depending upon the location of the interaction vertex. Track counting for individual γ-ray cascades is possible if the interaction vertex is in, or upstream of, the target module, i.e. for a "target jet". For a "calorimeter jet", i.e., the interaction vertex located inside the calorimeter module, individual cascades are not usually resolved, and track counting is done for the collective family of cascades.

5.1 Individual cascades in a "target jet"

The photons emanating from a target jet are geometrically separated in the calorimeter, so ΣE_γ can be obtained by summing the measured energies E_γ of the individual cascades. The energy of a photon-initiated cascade is determined in the traditional manner by comparing the observed number of cascade electrons within a circle of radius r (12.5–100 μm) about the cascade axis with numerically calculated curves based on three-dimensional cascade theory [12]. (Examples of calculated curves and data are shown in fig. 6). In this theory, the number of cascade electrons N as a function of the initial photon energy E_γ, depth t, and radial distance r satisfies the similarity relation

$$N(E_\gamma, r, t) = N\left(\frac{E_\gamma r}{K}, t\right). \tag{3}$$

provided that $E_\gamma r / K \ll 1$, where K is the scattering constant ($K = 19.6$ MeV in Pb). This similarity relation, the so-called "core approximation", is valid for the
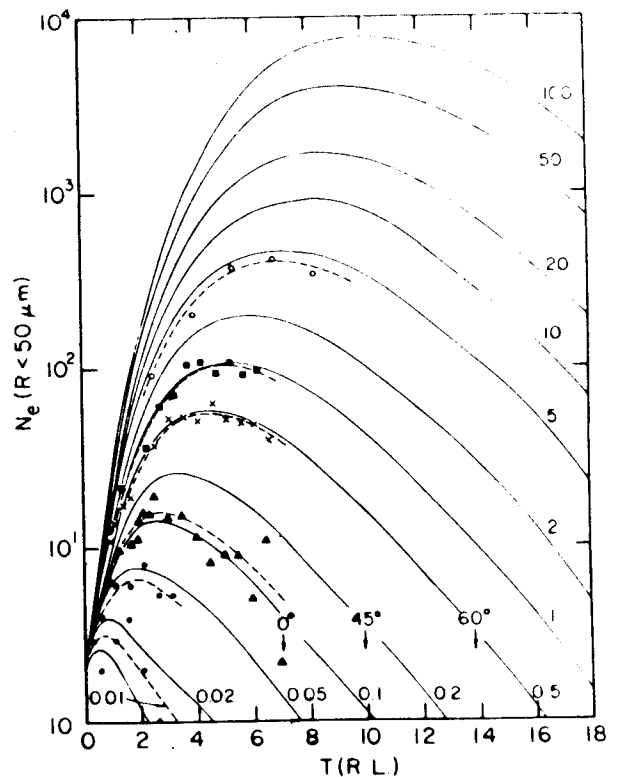

Fig. 6. Longitudinal development for cascades initiated by gamma rays. This family of sample calibration curves gives the number of cascade electrons N between radii $R_1 = 0$ and $R_2 = 50$ μm vs depth t in radiation lengths for a vertically incident cascade. The curves are labeled with the primary photon energy in TeV. The data points are from typical cascades, and the dashed lines indicate fitted transition curves. The arrows near the bottom show the maximum thickness of the calorimeter for photons incident at $0°$, $45°$, and $60°$ zenith angles.

small range of radii used in counting electrons for individual cascades. Individual energy measurements of the cascades in a family are possible if the individual photons are separated by distances greater than the track counting radius. The radial spread of electrons within a cascade is minimized by using lead in the calorimeter, while the distance between cascades is enhanced by the spacer module. Spatial resolution of the cascade cores permits their coordinate measurements and provides the emission polar angle θ_γ, from which the transverse momentum of photons, P_{T_γ}, is obtained through the relationship $P_{T_\gamma} = E_\gamma \sin \theta_\gamma$.

For well separated cascades, electron counting is typically carried out within a 50 μm radius. Track counting is not possible in the cores of very dense cascades. In such cases, a ring-area is chosen for track counting, and the data are compared with calculated cascade curves that eliminated the uncountably dense

cores. If the cascades overlap, track counting is done in the half- or quarter-circle sectors away from the neighboring cascades, and the numbers of tracks are scaled appropriately.

Multiple cascades closer together than about 12.5 μm are counted as one cascade, and the energy is allocated to each one in proportion to its core size around the shower maximum. Identification of individual cores in such collimated events are made in the upper emulsion layers of the calorimeter, where they can be distinguished with separation as small as 5 μm.

Both the individual energy and transverse momentum of gamma rays can usually be obtained for emission angles as small as 10^{-5} rad. In a typical event, the scanning for individual cascades is made for an area that contains cascades with emission angles up to 20 mrad. The threshold energy for essentially 100% probability for detection of a cascade is approximately 50 GeV, which corresponds to an average of 9 electron tracks within a 50 μm radius at shower maximum. During scanning, a cascade is operationally defined as a cluster of five or more quasi-parallel electron tracks within a radius of 50 μm that persists for at least two plates.

' . Cascades originating in a "calorimeter jet"

Photons emanating from calorimeter jets, or from vertices in the target layers very near the calorimeter, do not generally produce geometrically separated cascades. The energy determination procedure for these superimposed cascades is essentially the same as for individual cascades, except that track counting is performed over a single, larger radius (typically 200 μm) and a different set of cascade calibration curves is used. Such curves are generated numerically by superposing cascades initiated by individual photons [13]. The lateral spread is determined from both the transverse momentum distribution of the parent pions and the spread of cascade electrons in the electromagnetic process. The cascade model which simulates particle production based on accelerator results [14], is consistent with Fermilab electron calibration data [15]. Rapidity and transverse momentum distributions that assume scaling in the fragmentation region (limiting fragmentation [16]) are used. An alternative model that assumes scaling violations chosen to be consistent with data from 400 GeV proton experiments at Fermilab [17], cosmic ray experiments around 40 TeV [18,19], and recent 150 TeV SPS collider experiments at CERN [20] does not affect the power curves appreciably, as long as the same average inverse momentum $\langle P_T \rangle = 400$-500 MeV/c is used. The 200 μm radius was chosen to be both practical for track counting and reasonably insensitive to the choice of the empirical models. A typical family of cascade curves for a radius of 200 μm is shown with sample data in fig. 7.
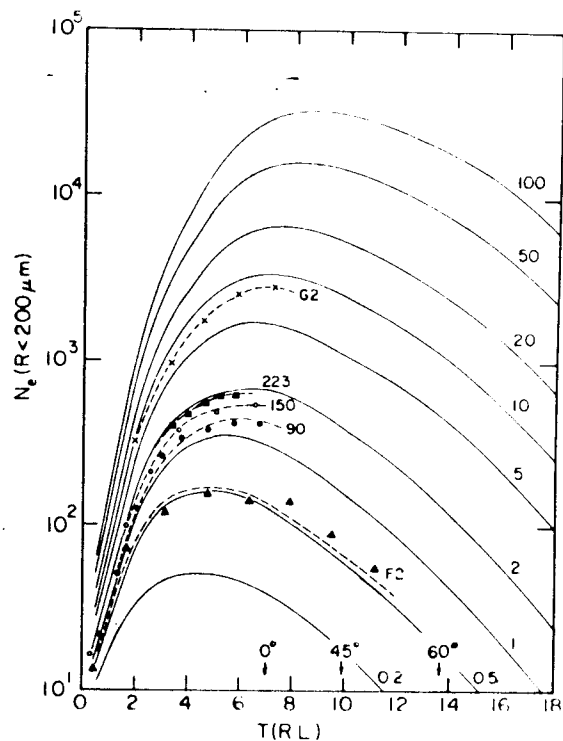

Fig. 7. Longitudinal development for "Pb jet" cascades initiated by protons. These transition curves are used for the analysis of events interacting in the calorimeter. This sample family gives the number of electrons between $R_1 = 0$ and $R_2 = 200$ μm for vertically incident cascades. The notation is the same as that used in fig. 6.

6. Energy resolution

Cascade energies are determined by minimizing the deviations of the measured points from the calculated cascade transition curves. The shower maximum is defined as the maximum of the calculated curve that best fits the data. Both the number of electrons at shower maximum and the total track length in a fixed radius are approximately proportional to the cascade energy. The total track length exhibits essentially Poisson fluctuations, so the accuracy of the energy measurement is proportional to $1/\sqrt{E_\gamma}$. However, fluctuation in the number of electrons at shower maximum is known to exceed Poisson fluctuations. A calibration experiment [15] using Fermilab electron beams up to 300 GeV has shown that the energy resolution from track counting in emulsion chambers similar to the JACEE design will vary from about 30% to 15% as the cascade energy increases from 50 to 300 GeV. In principle, better accuracy is expected for higher energy cascades. However, it is difficult to obtain energy resolution better than about 10%, because of errors in the track counts. Such errors result from the practical necessity of
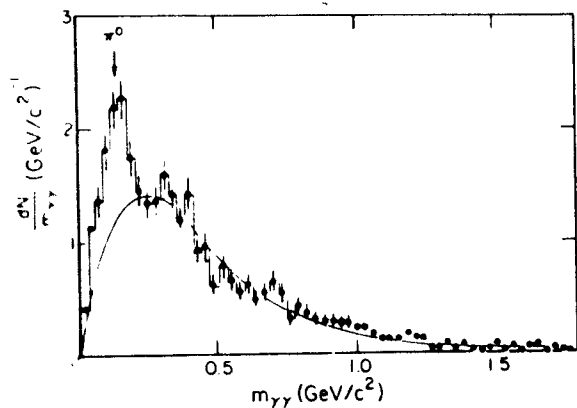
Fig. 8. Histogram showing the two-photon invariant mass distribution obtained for all possible pairings of observed gamma ray initiated cascades in a single target event. The solid curve represents a Monte Carlo simulation based on random pairings of the experimentally observed cascades. The width of the peak at the π^0 mass is 32%, which implies that the energy resolution for individual cascades is about 22%.

during counting for very dense cascades, from inaccuracies due to obscuration of tracks in cascades having large inclination angles, and from changes in track grain density due to local variations in emulsion sensitivity.

The invariant mass distribution of gamma ray pairs has been used to check the cascade energy measurements. A sample distribution for a proton primary is shown in fig. 8. The individual cascade energies range from 30 GeV to about 8 TeV in a single event. The exponential photon energy distribution [18] ($\sim 10E_\gamma/\Sigma E_\gamma$) indicates that the average energy of the photons in this sample is around 100 GeV. The width around the pion peak at 135 MeV/c^2 is about 32% which corresponds to an energy resolution of about 22% for individual cascades from neutral pion decay. These results are consistent with the Fermilab calibration data [15].

The accuracy of determining the total gamma ray energy, ΣE_γ, has been evaluated by Monte Carlo simulations which show that the maximum spread in ΣE_γ for target jets is about 25%. Secondary interactions in the calorimeter degrade the energy resolution, but careful measurements of cascade coordinates can predict the location of many cascades, so the effects of secondary interactions can be minimized. For complete removal of secondary interactions, the resolution in ΣE_γ can be as good as 10%, as illustrated in fig. 9 for carbon (acrylic plate) interactions.

For calorimeter jets, the resolution obtained by measuring ΣE_γ in a single track counting circle of 200 μm has been estimated via Monte Carlo simulations to account for the overlapping of individual cascades. A sample result is shown in fig. 10 for the interactions in Pb. The standard deviation of this distri-
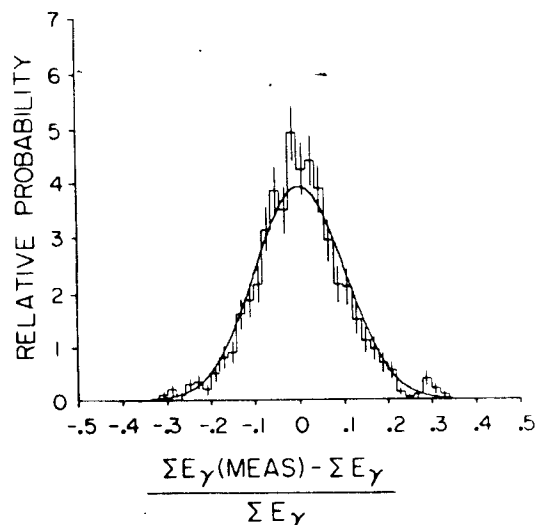

Fig. 9. Energy resolution obtained for proton–carbon interactions by summing individual gamma rays, which is the method used for events occurring in the target section of the chamber. The data points are from a Monte Carlo simulation based on the experimental data for multiplicity and energy distribution, with energy resolution for individual gamma rays taken to be 22%. The solid curve represents a Gaussian distribution with $\sigma = 0.10$.
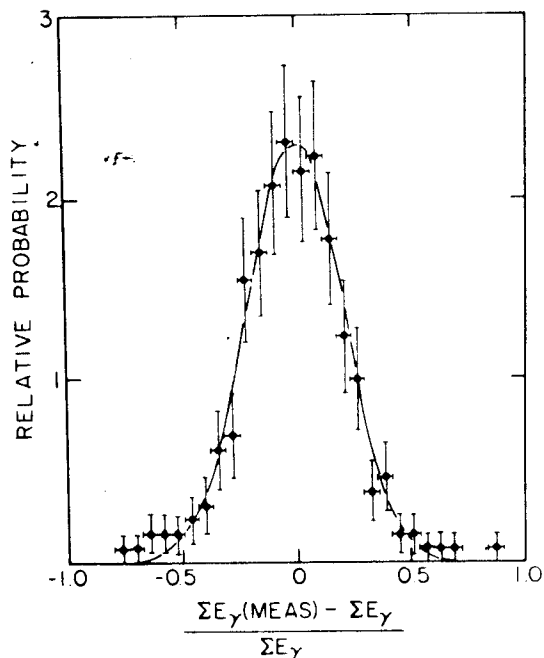

Fig. 10. Energy resolution obtained for proton–lead interactions by counting the number of tracks within a 200 μm circle, which is the method used for calorimeter (Pb jet) events where individual cascades cannot be resolved. The data points are from a Monte Carlo simulation with $k_\gamma > 0.1$ and $\Sigma E_\gamma > 1$ TeV, with secondary interactions included. The solid line represents a Gaussian distribution with $\sigma = 0.21$.

bution is 21%. A similar calculation for helium-lead interactions gives a standard deviation of 24%.

Overall, a reasonable estimate of the resolution of ΣE_γ in the JACEE chambers is better than 25%.

7. Geometrical efficiency factor

Determination of the primary energy spectrum requires knowledge of both the event energies and the collection efficiency of the detector exposures for each primary species. In order to be detected in the JACEE apparatus, a primary nucleus must interact in the emulsion chamber. Therefore, the collection factor depends on both the geometrical aperture and the number of interaction mean free paths along the primary trajectory in the apparatus, i.e., on both the mass and angle of incidence of the primary particle.

The geometrical efficiency factor $G(Z)$, for a nuclear species of charge Z, is a convolution of the geometrical acceptance of the chambers and the probability P that the cosmic ray species will interact in the detector. For a given species, G is given by

$$G = \int dx \int dy \int_0^{\theta_L} \sin\theta \cos\theta \, d\theta$$

$$\times \int_0^{2\pi} d\phi P(x, y, \theta, \phi),\qquad(4)$$

where θ_L is the maximum accepted zenith angle, ϕ is the azimuth angle, and x and y define the cross sectional area of the detector. The values of $G(Z)$ have been calculated by Monte Carlo simulations, with interactions separately identified in the target, cal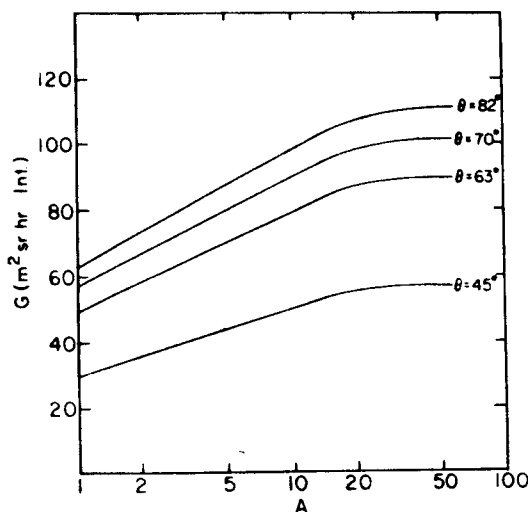orimeter, and external portions of the apparatus. Fig. 11 illustrates the calculated dependence of $G(Z)$ on the selected zenith angle θ_L.

Fig. 11. Calculated dependence of the geometrical efficiency factor G on incident zenith angle θ and primary mass number A for the accumulated JACEE exposure.

8. Primary spectrum analysis

The measured energy spectrum of ΣE_γ is a convolution of the primary cosmic ray spectrum with the energy response function of the detector. The latter depends on the distribution of partial inelasticity k_γ, which relates ΣE_γ to the primary energy E_0 by

$$\Sigma E_\gamma = k_\gamma E_0.\qquad(5)$$

The coefficient k_γ has a broad distribution ($\sigma(k_\gamma) \sim 50\%$), and the uncertainty in E_0 for an individual event is correspondingly large. However, there is a unique relation (simple scale shift) between the ΣE_γ spectrum and the corresponding primary spectrum, as long as the spectral index and the characteristics of the interactions do not change substantially over the observed energy range. (A primary spectrum index change would be reflected in ΣE_γ spectrum, but the transition energy would be broader.)

To avoid confusion in the discussion below, we will use E_m to represent ΣE_γ, k to represent k_γ, and the conventional symbol γ will be used for the cosmic ray spectral index, i.e., the slope of the integral energy spectrum.

When the differential primary (E_0) spectrum of a cosmic ray species is given by the simple power law relation

$$g(E_0) \, dE_0 = I_0 E_0^{-\gamma-1} \, dE_0,\qquad(6)$$

the differential spectrum (E_m) measured by an emulsion chamber is given by

$$G(E_m) \, dE_m = dE_m \int_k \int_{E_0} f(k) \, dk$$

$$\times I_0 E_0^{-\gamma-1} \, dE_0 \delta(E_m - kE_0)$$

$$= I_0 E_m^{-\gamma-1} \, dE_m \int_0^1 k^\gamma f(k) \, dk.\qquad(7)$$

Therefore, the measured spectrum has the same slope as the primary spectrum, but the normalization is changed by the factor

$$F(\gamma) = \int_0^1 k^\gamma f(k) \, dk.\qquad(8)$$

This result holds for any $f(k)$ as long as that distribution is independent of energy [21].

We can determine the energy scale shift between the primary (E_0) spectrum and the measured (E_m) spectrum by finding the energies $E_m = E_2$ and $E_0 = E_1$ where the integral intensity of the E_m spectrum equals that of the E_0 spectrum:

$$\int_{E_2}^\infty G(E_m) \, dE_m = \int_{E_1}^\infty g(E_0) \, dE_0.\qquad(9)$$

Putting eqs. (6) and (7) in this relation we get

$$(E_2/E_1)^\gamma = \int_0^1 k^\gamma f(k) \, dk,$$ (10)

or

$$E_2 = E_1 \left(\int_0^1 k^\gamma f(k) \, dk \right)^{1/\gamma} \equiv C(k, \gamma) E_1.$$ (11)

The conversion factor,

$$C(k, \gamma) = \left(\int_0^1 k^\gamma f(k) \, dk \right)^{1/\gamma},$$ (12)

represents the energy scale shift required to go from the E_0 spectrum to the $E_m = \Sigma E_\gamma$ spectrum. Its reciprocal $(C(k, \gamma))^{-1}$ represents the multiplicative factor to be applied to ΣE_γ values to obtain the E_0 spectrum. The value of $C(k, \gamma)$ is a stable function of $f(k)$ and γ, provided that γ is greater than unity, which is the case for high energy cosmic ray spectra. Variations in the distribution $f(k)$ at small k have negligible effect on $C(k, \gamma)$.

The effective energy region of E_0 corresponding to the observation of a specified E_m is readily understood by similarly defining the average of $1/k'$ where the "prime" indicates the bias caused by the power law energy spectrum:

$$B(k, \gamma) \equiv \langle 1/k' \rangle = \frac{\int_0^1 k^{\gamma-1} f(k) \, dk}{\int_0^1 k^\gamma f(k) \, dk}.$$ (13)

Note that $B(k, \gamma)$ is always smaller than $(C(k, \gamma))^{-1}$ (although they are very close in numerical value), due to the bias from the power spectrum and the E_m trigger. It is incorrect to use $B(k, \gamma)$ instead of $(C(k, \gamma))^{-1}$ for the energy scale shift of E_m to get the E_0 spectrum, because $B(k, \gamma)$ gives only an "effective" average value of $1/k'$.

It should also be noted that the reciprocal of the average of the observed k' values, $\langle k' \rangle^{-1}$, should not be used for either $C(k, \gamma)$ or $B(k, \gamma)$. Because of the E_m trigger, the distribution of k' values derived from studies of the interaction characteristics of detected events, will be an average of biased k values, i.e., $\langle k' \rangle$ given by

$$A(k, \gamma) \equiv \frac{\int_0^1 k^{\gamma+1} f(k) \, dk}{\int_0^1 k^\gamma f(k) \, dk}.$$ (14)

The difference in the moment factors for eqs. (13) and (14) causes the inequality relationship, $A(k, \gamma)^{-1} \neq B(k, \gamma)$, due to the fact

$$A(k, \gamma) \cdot B(k, \gamma) = \langle k' \rangle \cdot \langle 1/k' \rangle > 1.$$ (15)

An observed (E_m) spectrum in the energy region $E_m(1)-E_m(2)$ should be transformed into the E_0 spec-

trum by using $(C(k, \gamma))^{-1}$ for the energy scale shift of the spectrum, and by $B(k, \gamma)$ for the energy scale shift of the observed E_m energy range to the corresponding range of the primary spectra, i.e.,

$$E_m(1)B(k, \gamma)-E_m(2)B(k, \gamma).$$

9. Effect of uncertainties in the inelasticity distribution

In calculating the coefficients $C(k, \gamma)$, $B(k, \gamma)$, and $A(k, \gamma)$ we need the partial inelasticity distribution $f(k)$. The $f(k)$ can be derived from the total inelasticity distribution $f_0(K)$ by two different assumptions about the gamma ray/charged hadron energy partition: (1) binomial fluctuation in isospin space and (2) uniform fluctuation in isospin space. Although the physical bases for the two assumptions are different, and even though they yield differences in $f(k)$ at small k values, calculated results for the coefficients $C(k, \gamma)$ and $B(k, \gamma)$ are practically the same for both assumptions. This is due to the suppression factor (moment power) existing in the integrand of eqs. (12) and (13). The total inelasticity distribution function $f_0(K)$ has been conventionally considered uniform if integrated over the P_T of the protons [13] (Case I). Deviations from this are also considered by using the inclusive data of protons at $P_T = 300$ MeV/c obtained from 100 GeV proton-nucleus experiments of FNAL (Case II) [22].

$$f_0(K) = \frac{dN}{dK} = \sigma_0(A)$$

$$\times \frac{\exp\left[\alpha(A) \left\{ (1 - K)^2 - (m^2 + \langle P_T^2 \rangle)/E_0 \right\}^{1/2} \right]}{\left\{ (1 - K)^2 - (m^2 + \langle P_T^2 \rangle)/E_0 \right\}^{1/2}},$$ (16)

where m and P_T are the proton mass and transverse momentum, and A denotes the atomic number of the target nucleus. The normalization factor $\sigma_0(A)$ is determined from the original invariant cross section. The nuclear effect is fully taken into account, and the factor $\alpha(A)$ is defined by

$$\alpha(A) = 1.507 - 0.622A^{0.185},$$ (17)

which fits well to all experimental data of Barton et al. for $1 < A < 207$ [22]. This formula gives larger $C(k, \gamma)$ values than the standard (uniform) $f_0(K)$ distribution of Case I.

Numerical results for the $C(k, \gamma)$ conversion factor, taking into account secondary interactions in the JACEE chambers, are given in table 5. Values for helium primaries are subject to some ambiguities depending on the collision model, for which we have used the wounded nucleon model [23].

The assumption that the inelasticity distribution in

Table 5

Numerical values of $C(k, \gamma)$ for a primary energy spectrum with $\gamma = 1.7$

Interaction	$C(k, \gamma)$ Case I	$C(k, \gamma)$ Case II
Proton–carbon	0.22	0.25
Proton–lead	0.24	0.29
Helium–carbon	0.16	0.18
Helium–lead	0.17	0.21

proton or helium–nucleus interactions remains approximately independent of incident energy is equivalent to the hypothesis of limiting fragmentations [16]. Data on the inelasticity distribution at different energies permit us to examine the validity of this assumption for our use. However, use of eq. (17) for Case II is valid for the data by Barton et al. [22] at 100 GeV and Whalley et al. [24] at 400 GeV, while the 24 GeV data by Eichten et al. [25] and the CERN ISR data at 1.8 TeV by Albrow et al. [26] are considered for Case I. The ambiguity in conversion factors caused by different accelerator results remains within 20%.

Data on inelasticities around 150 TeV from the $\bar{p}p$ collider are not directly available so far. However, we can evaluate the energy dependence of $\langle K \rangle$ in elementary nucleon collisions by comparing the total energy flow for secondary particles within the measured rapidity space at two energies. e.g., 1.8 TeV from the ISR [27] and 150 TeV from the SPS collider [20]. Taking into account the reported abundance of gamma rays at 150 TeV, we get less than 20% increase in average inelasticity as the primary energy E_0 increases from 1.8 to 150 TeV. This implies that the increase of average partial inelasticity could be slower than $E_0^{0.04}$. The ambiguity corresponding to the measured spectral index for primary cosmic rays is estimated to be less than 0.075 for $\gamma = 1.8$. Some reports [28] indicate a much smaller change, less than 10% for $\langle K \rangle$, (up to 405 TeV ($\sqrt{s} = 900$ GeV)) which leads to negligible correction for the spectral index obtained by the analysis method described here.

10. Results for proton and helium spectra

The integral proton and helium spectra shown in fig. 12 were obtained by applying the techniques described herein to the JACEE data. Several different sets of the JACEE data with different threshold energy and exposure factors are shown here with subthreshold data points (down to 80% of E_{th}) to illustrate characteristic detection efficiencies. For comparison, the results from the PROTON satellite experiments [4] and the highest energy balloon data [6] are also given. No indication of a change in the spectral index for protons has been
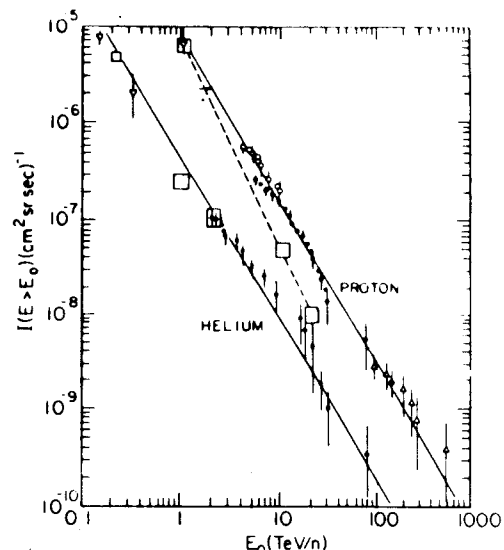

Fig. 12. Integral energy spectra for protons and helium nuclei. The large, open squares represent data of Grigorov et al. [4] from the PROTON satellites. The previous highest energy balloon data, Ryan et al. [6] are indicated by the inverted triangles. Different sets of JACEE data, which were combined to produce this figure, are indicated by different symbols (open and full circles, and normal triangles).

observed with the JACEE emulsion chambers up to at least 100 TeV. The best fits to power law spectra above 1 TeV in units of $(\text{cm}^2 \text{ sr s})^{-1}$ have been reported [2] as

protons: $I(> E) = 6.9 \times 10^{-6} E^{-1.81 \pm 0.13}$,

helium: $J(> E) = 2.9 \times 10^{-7} E^{-1.83 \pm 0.20}$ (18)

11. Concluding remarks

Application of the described analysis techniques to balloon-borne emulsion chambers has permitted measurement of the primary cosmic ray proton and helium energy spectra over the approximate range 5–500 TeV. This dynamic range was made possible by the large geometric aperture of the emulsion chambers. The experimental methods rely on proven characteristics of both hadronic and electromagnetic interactions. This method is equally valid for much higher energies. Spectral measurements up to about 10^{16} eV could be achieved with a larger area and/or longer exposures of apparatus similar to the JACEE chambers. This would allow examination of the "knee" in the cosmic ray spectrum [29], in addition to covering the energy region where protons and helium nuclei are expected to exhibit steeper spectra as a result of leakage from the local confinement volume in the galaxy [30].

The emulsion chamber method is also applicable to both charge and energy determinations for nuclei heavier

than helium Some special information, e.g., the dependence of the inelasticity distribution on atomic mass number, must be known for accurate energy estimates of heavy nuclei. Such information can be obtained directly from studies of nucleus–nucleus interactions in the chambers, which will be considered in a subsequent report

References

[1] T H Burnett et al., Phys. Rev. Lett. 50 (1983) 2062.

[2] T H Burnett et al., Phys. Rev. Lett. 51 (1983) 1010.

[3] The emulsion chamber technique was introduced by M.F. Kaplon, B Peters, H.L. Reynolds and D.M. Ritson, Phys. Rev. 85 (1952) 295 and developed mainly by Japanese groups, e.g. O. Minakawa et al., Suppl. Nuovo Cimento 8 (1958) 761. and K. Niu et al., Prog. Theor. Phys. 46 (1971) 1644

[4] N I Grigorov, Yu.V. Gubin, I.D. Rapoport, I.A. Savenko, B M Yakovlev, V.V. Akimov and V.E. Nesterov. 12th ICRC Conf. Papers. Hobart, Tasmania (University of Tasmania. 1971) vol. 5, p. 1746; N.L. Grigorov, N.A. Mamontova, I.D. Rapoport, I.A. Savenko, V.V. Akimov and V.E. Nesterov, op. cit., p. 1752; N.L,. Grigorov, I.D. Rapoport, I.A Savenko, V.E. Nesterov and V.L. Prokhin, op cit., p 1760.

[5] W K H Schmidt, K. Pinkau, U. Pollvogt and R.W. Huggett. Phys. Rev. 184 (1969) 1279; K. Pinkau, U. Pollvogt, W K.H Schmidt and R.W. Huggett, Acta. Phys. Hungar. 29 suppl. 1 (1970) 291.

[6] M Ryan, J.F. Ormes and V.K Balasubrahmanyan, Phys Rev. Lett. 28 (1972) 985; and erratum op. cit., p. 1497.

[7] V K Balasubrahmanyan and J.F. Ormes, Astrophys. J 186 (1973) 109

[8] See R L Fleischer, P.B. Price and R.M. Walker, Nuclear

Tracks in Solids (University of California Press, Berkeley, 1975).

[9] C.F. Powell, P.H. Fowler and D.H. Perkins, The Study of Elementary Particles by the Photographic Method (Pergamon Press. New York, 1959).

[10] W.H. Barkas, Nuclear Research Emulsions (Academic Press, New York, 1963).

[11] T. Hayashi and T. Doke, Nucl. Instr. and Meth. 174 (1980) 349.

[12] J. Nishimura. Prog. Theor. Phys. Suppl. 32 (1964) 72. Handbuch der Physik, vol. 62 (Springer, Berlin, 1967)

[13] S. Dake (Kobe University, Kobe, Japan). unpublished (1980); S. Dake et al., 15th ICRC Conf. Papers, Plovdiv, Bulgarian Academy of Sciences (1977) vol. 7, p. 322

[14] T. Tabuki, Prog. Theor. Phys. Suppl. 76 (1983) 40.

[15] N. Hotta, H. Munakata, M. Sakata, Y. Yamamoto, S. Dake, H. Ito, M. Miyanishi, K. Kasahara, T. Yuda, K. Mizutani and I. Ohta, Phys. Rev. D22 (1980) 1.

[16] J. Benecke, T.T. Chou, C.N. Yang and E. Yen, Phys. Rev. 188 (1969) 2159.

[17] C. Bromberg, T. Ferbel, P. Slattery, A.A. Seidel and J.C. Van der Verde, Nucl. Phys. B107 (1976) 82.

[18] T.H. Burnett et al., in Proton–Antiproton Collider Physics 1981, AIP Conf. Proc. (American Institute of Physics, New York, 1982) vol. 85, p. 552.

[19] S. Tasaka et al., Phys. Rev. D25 (1982) 1765.

[20] K. Alpgard et al. (UA5 Collaboration). Phys. Lett. B 107 (1981) 310.

[21] S. Hayakawa, J. Nishimura and Y. Yamamoto, Prog. Theor. Phys. Suppl. 32 (1964) 104.

[22] D.S. Barton et al., Nucl. Phys. D27 (1976) 2580.

[23] A. Bialas et al., Nucl. Phys. B111 (1976) 461.

[24] M.R. Whalley et al., University of Michigan Report No UM HE79-14 (1979) unpublished.

[25] T. Eichten et al., Nucl. Phys. B44 (1972) 333.

[26] M.G. Albrow et al., Nucl. Phys. B54 (1973) 6.

[27] W. Thome et al., Nucl. Phys. B129 (1977) 365.

[28] D.R. Ward (UA5 Collaboration), in Physics in Collisions V, ed., L. Montanet (Frontier, Yvette, France, 1985).

[29] A.M. Hillas, 16th ICRC Conf Papers, Kyoto, Japan (Institute for Cosmic Ray Research, University of Tokyo, Tanashi, Tokyo 188, Japan, 1979) vol. 8, p. 7.

[30] G.B. Yodh, in: Cosmology and Particles eds., J. Audouze et al. (First Moriond Astrophysics Meeting, Frontieres-Dreux, 1981).